DOI: 10.1002/ejic.201000804

# Synthesis of Two-Dimensional Carbon and Carbon–Metal Nanocomposites Using a Natural Cellular Material as the Carbon Precursor

**Fengbin Li,[a] Ling Li,[b] Xingzhi Liao,[a] Ling Tong,[a] Zhiquan Chen,[a] and Yong Wang*[a]**

**Keywords:** Organic-inorganic hybrid composites / Carbon / Cellulose / Nanoflakes / Nanoparticles / Nanocomposites / Pyrolysis

Two-dimensional carbon nanostructures, including carbon nanoflakes that are formed from the disassembly of carbon foams and carbon–metal composites, were directly synthesized using the stem pith of the rice-paper plant (SPRP) as the carbon precursor and also the synthesis template. SPRP has a foamlike porous structure. SPRP was pyrolyzed to prepare carbon foam with ultralow apparent density, and this foam was ruptured to produce carbon nanoflakes with a lateral size up to hundreds of micrometers and a thickness of approximately 100 nm. Palladium and platinum were added to the SPRP foams by wet impregnation, and the impregnated foams were subsequently converted into composites of metal nanoparticles and carbon in the form of foams or nanoflakes. The composites were characterized using electron microscopy, energy-dispersive spectroscopy, X-ray diffraction, and Raman spectroscopy. The metal nanoparticles were found to be highly crystalline with diameters in the range of several tens of nanometers (palladium) and several nanometers (platinum), and were uniformly distributed throughout the carbon nanoflakes. The amount of metal in the composite was tunable by changing the impregnation time and the concentration of the impregnation solution.

## Introduction

Carbon-based materials have long been widely used in industries and intensively studied in laboratories for various purposes because of their superior thermal and chemical stability, as well as their unique electronic properties. With the recent discoveries of fullerene,[1] carbon nanotubes,[2] and graphene,[3] carbon-based materials with nanoscopic features – for instance, nanoporous carbon and low-dimensional carbon structures – have attracted ever-increasing interest that arises from their additional properties unseen in their bulk analogues.[4–6] Carbon nanomaterials can be obtained through different routes that can be simply classified into two categories: physical and chemical methods. Chemical routes are advantageous over physical ones, mainly in terms of cost efficiency and the possibility of mass production.[7–9] In addition, mankind has a long history of carbonizing wood and other agricultural wastes for the production of carbon products (e.g., charcoal and activated carbon), predominantly for use as fuels and absorbents.[10–15] In recent years, biosourced carbon has expanded its uses as gas-storage media,[16–18] capacitors,[19] and battery-electrode materials[20] for the sake of a low-cost and stable supply of carbon precursors. On the other hand, as many biomaterials possess regular, subtle architectures on different scales from bulk down to the nanometer size, it is well documented that, in using a large variety of biomaterials as templates,[21–26] it is possible to produce inorganic replica of their fine structures. Previously, we have successfully prepared titanium oxide replica from various biotemplates including cotton fibers,[27] pollen grains,[27] and swim bladders[28] with the aid of supercritical carbon dioxide. Similarly, it is highly attractive to discover suitable biomaterials as carbon precursors to fabricate carbon materials with regular structures. We and others have reported some works on the conversion of nano- and microstructured biotemplates to carbon counterparts with corresponding fine structures through the direct carbonization method.[29–31] Biosourced carbons have superior advantages over fossil-based carbon materials in some aspects. First, biosourcing of carbon is usually low in cost and, more importantly, renewable, and therefore environmentally friendly. Second, many biomaterials are mainly composed of cellulose and semicellulose. They can be directly pyrolyzed to carbon in inert environments without any pretreatment. Third, most biomaterials have specific naturally endowed structural features that can be transferred to the corresponding carbon materials, and no template is needed as in the synthetic approach. Last but not least, there is a large amount of active groups – for instance, hydroxy, carbonyl, and amino groups – in most kinds of biomaterials. These active groups are able to bind metal ions and other chemical spe-

---

[a] State Key Laboratory of Materials-Oriented Chemical Engineering,
College of Chemistry and Chemical Engineering,
Nanjing University of Technology, Nanjing 210009, Jiangsu, P. R. China
Fax: +86-25-8317-2292
E-mail: yongwang@njut.edu.cn
[b] School of Life Sciences, Lanzhou University,
Lanzhou 730000, Gansu, P. R. China

cies through complexation and/or electrostatic interactions. The metal-ion-bound biomaterials can further be converted to composites of carbon and metals or metal oxides.

The first key point for the preparation of structured biosourced carbon is to discover suitable biomaterials with the desired structures. In the present work, we have investigated the stem pith of the rice-paper plant (*Medulla tetrapanacis*), which is denoted as SPRP below. SPRP has a closed-cell foamlike architecture, and consequently an ultralow density. By using SPRP as the biotemplate and carbon precursor simultaneously, we obtained two types of carbon materials: carbon foams and carbon nanoflakes. Because of their ultralow weight and applications as high-temperature thermal insulators as well as highly thermally conductive heat sinks, considerable efforts have recently been devoted to carbon foams, but predominantly starting from fossil-based precursors plus an additional foaming process.[32–37] Carbon nanoflakes are expected to find applications as fillers to improve the mechanical strength of materials and to enhance their electrical and thermal conductivity. Moreover, since carbon-supported metal nanoparticles are widely used as catalysts for organic synthesis and electrode materials for fuel cells and lithium-ion batteries,[38,39] the major efforts in the present work are dedicated to the incorporation of metal precursors including palladium and platinum in biosourced carbon foams and nanoflakes for the preparation of metal–carbon composites.

## Results and Discussion

### Characterization of SPRP Fibers

We first used a FTIR spectrometer with an attenuated total reflection (ATR) module to examine the chemical nature of the SPRP fibers. As shown in Figure 1, evident peaks at positions of 1239, 1434, and 1732 cm$^{-1}$ can be seen clearly, which should be assigned to C–O bond vibration, COO– symmetric stretching vibration, and the stretching vibration of free C=O groups, respectively.[40] The peak present at 3344 cm$^{-1}$ is characteristic of –OH groups. Therefore, we conclude that there are plenty of "active" species in the pristine SPRP fibers including carboxylic, hydroxy, carbonyl groups, and so on, that have the capability of strong complexation to bind metallic ions.

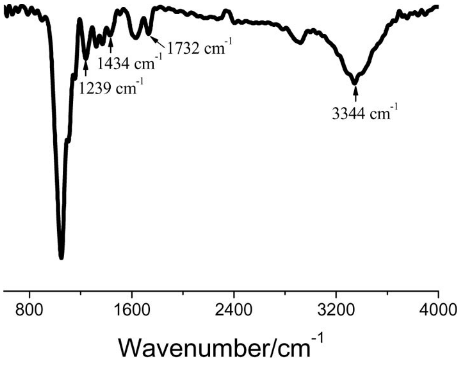

Figure 1. FTIR-ATR spectrum of pristine SPRP fibers.

We then investigated the morphology and structure of pristine SPRP fibers using scanning electron microcopy (SEM). SPRP fibers are macroporous and possess a closed-cell foamlike architecture, as can be observed under low-magnification SEM. The size of the foam cells is around 100 µm in diameter and composed of thin flakes, as shown in Figure 2 (a and b). Because of their highly porous structure, SPRP fibers are extremely light and have an apparent density of approximately 0.08 gcm$^{-3}$, and due to their relatively hydrophobic nature, SPRP fibers can also remain afloat on the surface of water for days.

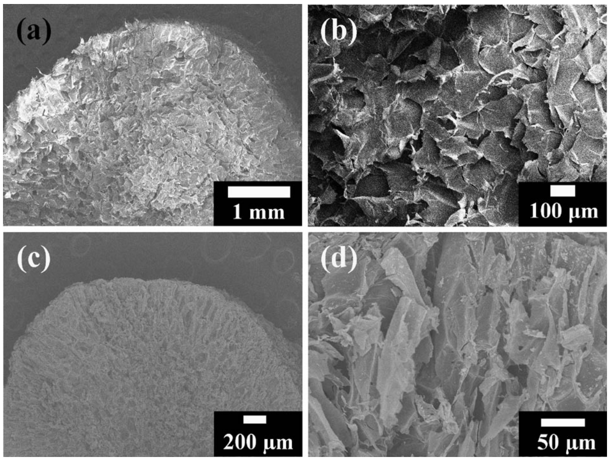

Figure 2. Cross-sectional SEM images of (a, b) pristine SPRP and (c, d) carbonized SPRP.

### Carbon Foams and Carbon Nanoflakes

SPRP can be carbonized easily under the protection of inert gas at high temperature. In the carbonization of natural cellular materials, complicated inter- and intramolecular reactions including devolatilization, decomposition, cyclization, crosslinking, and so on take place, thereby resulting in the loss of labile and low-molecular-weight components but leaving the carbon-rich frameworks. The carbonized products maintain the original shape and profile of SPRP fibers, as shown in Figure 3. There is a significant volume shrinkage (ca. 80%), as well as a weight loss of also approximately 80%, thus indicating that carbonized SPRP preserves the low density (ca. 0.08 gcm$^{-3}$) of the pristine SPRP. We further examined the morphology of the carbonized SPRP with SEM. As can be seen in Figure 2 (c and d), the foamlike porous structure is also preserved well in the carbonized SPRP. When subjected to ultrasonication, most of the cells of the ground carbon foams were broken into pieces of fractured carbon flakes. The flakes are laterally large with a size of tens of micrometers but extremely thin with a thickness in the range 100–300 nm (Figure 4, a and b). The carbon nanoflakes are homogeneous and nonporous throughout their whole area, as revealed by TEM examinations (Figure 4, c and d). The above analysis indicates that the direct carbonization of SPRP is an effective way for the fabrication of low-weight carbon foams, which can be further disassembled into carbon flakes with nanometer-scale thickness.

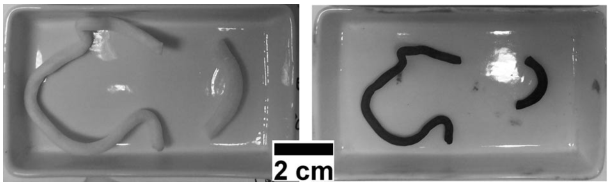

Figure 3. Photographs of the (a) pristine SPRP and (b) carbonized SPRP.

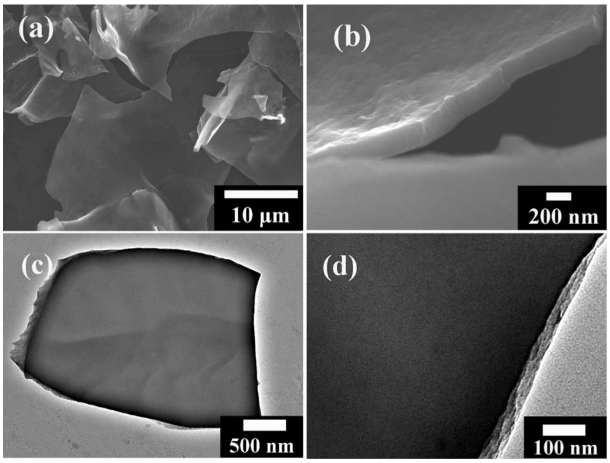

Figure 4. (a, b) SEM images and (c, d) TEM images of carbon nanoflakes of broken SPRP carbon foam.

### Carbon–Pd Composites

As we demonstrated above, there are considerable amounts of “active” carbonyl, carboxyl, and hydroxy groups on the surface of SPRP. These groups can bind metal ions through complexation and/or electrostatic interactions.[40] We expect that the metal-ion-bound SPRP will be converted to metal–carbon composites through the carbonization process. To this end, we first incorporated palladium precursors into SPRP through a simple wet impregnation method. In this method, short SPRP rods were immersed in a 1:1 water/ethanol solution of $Pd(OAc)_2$ in ethanol, which wet the SPRP pores well, then carbonized in nitrogen using the same procedure for the carbonization of the pristine SPRP. Similar to the carbonized products of pristine SPRP, the carbonized Pd-loaded SPRP preserves its macroscopic shape and structure accompanied by a significant volume shrinkage. The foamlike porous structure was also maintained as revealed by low-magnification SEM examination. However, under closer SEM observation, as shown in Figure 5 (a and b), we found there was a large amount of particles with diameters ranging from 10 to 40 nm on the surface of carbon nanoflakes prepared by carbonizing SPRP impregnated with 0.3 wt.-% $Pd(OAc)_2$ solution for 8 h. These nanoparticles were uniformly distributed throughout the entire surface, and were individually separated from each other and no coalescence of neighboring particles could be found. TEM results given in Figure 5 (c and d) further confirmed that nanoparticles were homogeneously dispersed throughout the entire area of the nanoflakes, and these nanoparticles, especially bigger ones, were roughly shaped, and entrapped in cavities that appeared in lighter color in contrast to the gray background of the carbon flakes, as shown in Figure 4 (d). We think the bubble-like cavities were caused by bubbling and erosion in softened or melt SPRP during the carbonization process by erosive gas released from the decomposition of the metal precursor at high temperature.

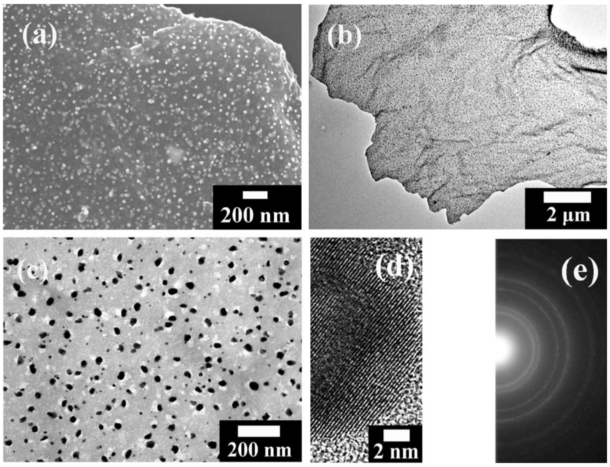

Figure 5. (a) SEM image, (b, c) TEM images, (d) HR-TEM image, and (e) SAED pattern of nanoflakes of carbonized SPRP impregnated with 0.3 wt.-% $Pd(OAc)_2$ solution for 8 h.

We performed elemental analysis on the carbonized products both from pristine and Pd-loaded SPRP using the energy-dispersive spectroscopy (EDS) detector attached to the SEM microscope, and found that the carbonized pristine SPRP contained only carbon and oxygen, whereas the carbonized Pd-loaded SPRP also had a substantial amount of palladium (data not shown), thereby indicating that nanoparticles absent on the carbonized pristine SPRP consisted of Pd. Furthermore, we conducted high-resolution TEM analysis of these nanoparticles. As shown in Figure 4 (d), we found these particles were single crystals, and their crystal lattice can be clearly recognized. The distance of the lattice constant is approximately 0.23 nm and corresponds to the (111) plane of elementary Pd. Therefore we can draw the conclusion that these nanoparticles are metallic palladium, and the carbonization of Pd-loaded SPRP leads to carbon–Pd composites. The crystalline nature of the Pd nanoparticles was further confirmed by selected area electron diffraction (SAED), although the SAED pattern of the carbon–Pd composite shows multiple concentric rings (Figure 5, e) instead of single-crystal-featured arrays of spots. This is because the diameter of the electron beam of our TEM, in the micrometer range, is much larger than the size of a single Pd nanoparticle, and it covers many particles in different orientations, thus resulting in a collective ringlike SAED pattern. The XRD pattern given in Figure 6 (a) of the carbon–Pd composite shows four strong crystalline peaks at 40.1, 46.7, 68.1, and 82.2°, which correspond, respectively, to the (111), (200), (220), and (311) planes of cubic-phase Pd according to the standard literature values reported for Pd (JCPDS, no. 65-2867), whereas in contrast, there are no obvious crystalline peaks present in pyrolyzed pristine SPRP.

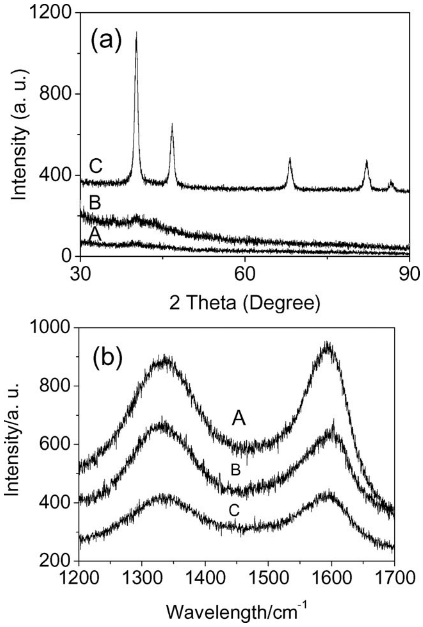

Figure 6. (a) XRD patterns and (b) Raman spectra of carbonized products of (A) pristine SPRP, (B) carbonized SPRP impregated in 1 wt.-% $NaPtCl_4$ solution for 24 h, and (C) SPRP impregated in 1 wt.-% $Pd(OAc)_2$ solution for 24 h.

Raman spectroscopy was used to characterize the pyrolysis products of pristine SPRP and metal-salt-loaded SPRP. As shown in Figure 6 (b), there are two broad bands centered around 1335 and 1594 $cm^{-1}$, respectively, which can be assigned to graphitic and disordered carbon, respectively, thereby indicating that pyrolysis of pristine and metal-salt-loaded SPRP at 600 °C results in partially graphitized carbon.[41,42]

## Tunability of Pd Content in Carbon–Pd Composites

The Pd content in the carbon–Pd composite from the pyrolysis of Pd-salt-loaded SPRP can be tuned over a relatively wide range, simply by changing the impregnation time and/or the concentration of the Pd-salt solution. Figure 7 (a–i) present the TEM and SEM images of carbonized SPRP flakes impregnated in Pd-salt solution with a concentration of 0.3% for different periods of time from 0.5 h up to 24 h. Clearly, the amount of Pd nanoparticles on carbon flakes steadily increases with the impregnation time. EDS measurements show that the amount of Pd in the composite increases from around 3 wt.-% for the sample with 0.5 h impregnation, to around 9 wt.-% for the sample with 2 h impregnation, and to around 14 wt.-% for the sample with 8 h impregnation, and finally reaches approximately 23 wt.-% after 24 h impregnation. The metal-ion-binding process is a liquid–solid reaction. Compared to the same reaction that takes place in a complete liquid system, Pd ions dissolved in ethanolic water take a longer time to be captured by the active groups present on solid SPRP templates. In addition, the hydrophobic nature of the SPRP surface further decreases the penetration of metal ions into SPPR although the ethanol used facilitates the transport of metal ions by wetting and swelling SPRP. Therefore, Pd ions gradually diffuse inside the SPRP foam and have access to the active groups in SPRP, and are subsequently captured by these active groups. It is a time-dependent, diffusion-controlled process. As a result, the amount of Pd ions captured increases with the impregnation time until saturation. There might be a metal-ion-concentration gradient distribution along the thickness of the SPRP cell wall, but it should be to a very limited degree since the cell wall is thin. In the subsequent carbonization step, further immigration of metal species takes place and neighboring metal ions aggregate and are converted to elemental metal nanoparticles, which both greatly eliminate the gradient distribution of metal nanoparticles along the carbon-flake thickness. As shown in Figure 7 (d), in which the cross section of a broken carbon flake is exposed, nanoparticles could be observed both inside the flakes and on both surfaces, and no gradient distribution of particles was noticed. It follows straightforwardly that more Pd ions captured by SPRP lead to more metallic Pd particles. Therefore, we can continuously tune the metal amount in the composites simply by

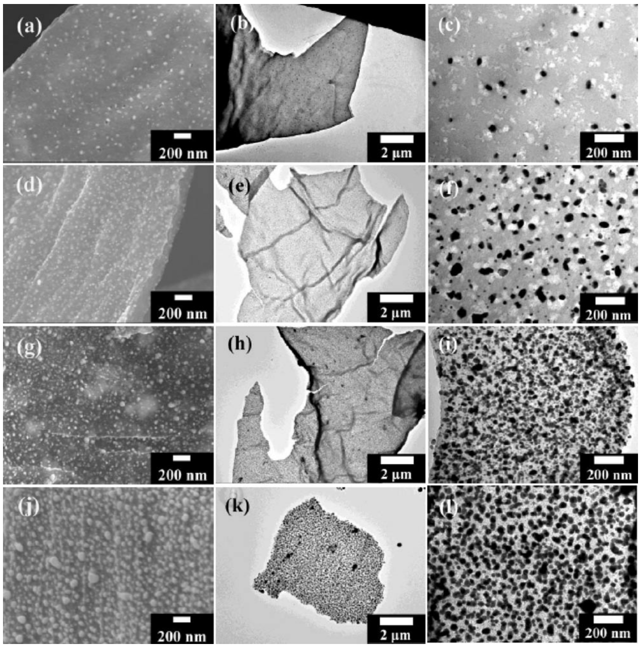

Figure 7. Electron-microscopy images of carbonized SPRP impregnated in 0.3 wt.-% $Pd(OAc)_2$ solution for (a, b, c) 0.5 h, (d, e, f) 2 h, and (g, h, i) 24 h; and electron-microscopy images of carbonized SPRP impregnated in 1 wt.-% $Pd(OAc)_2$ solution for (j, k, l) 24 h. (a, d, g, and j) SEM images; the others are TEM images.

changing the impregnation time. On the other hand, with the prolongation of impregnation time, the size of the Pd nanoparticles increases slightly as their size distribution is improved to some extent. This is probably because with longer impregnation time, Pd ions distribute on SPRP flakes more uniformly, which provides a more stable supply of Pd source to form Pd nanoparticles in the carbonization step.

Furthermore, the amount of Pd can also be controlled effectively by altering the concentration of the Pd-salt solution. For instance, Figure 7 (j, k, and l) display the TEM and SEM images of carbon–Pd composite derived from SPRP impregnated in 1 wt.-% Pd salt for 24 h. Compared with the one prepared from SPRP treated in 0.3 wt.-% Pd salt for the same period of time, SPRP impregnated in 1 wt.-% Pd salt gives many more Pd nanoparticles than that impregnated in 0.3 wt.-% Pd salt. As revealed by EDS determination, Pd content increases to about 40% for the sample prepared in 1 wt.-% Pd salt, whereas, as stated above, Pd content is 23 wt.-% for the one prepared in 0.3% Pd salt. This is because a higher concentration of Pd ions results in a stronger concentration contrast between that in the bulk solution and inside the SPRP, thereby driving more Pd ions to penetrate SPRP and react with its active groups in the same period of time. Consequently, a larger content of Pd in the carbonized sample was obtained.

### Carbon–Pt Composites

In addition, this method can be easily adopted for the fabrication of other carbon-supported noble metals, for instance, platinum. After replacing Pd salt with a suitable Pt salt, a carbon–Pt composite was prepared through the same impregnation and subsequent carbonization protocol. There is no difference in the macroscopical structure and morphology of the carbonized Pt-impregnated SPRP and carbonized Pd-impregnated SPRP or pristine SPRP. They all are black and take a shrunken but unbroken, foamlike form. Figure 8 (a and b, c) give the SEM and TEM images of the carbon–Pt sample, respectively. TEM images show that there are particles with a size of around 3–5 nm on the carbon flake, whereas under SEM the carbon flakes are very smooth and no particles can be detected because of the limited resolution of SEM. EDS measurements indicate that the pyrolysis product of the Pt-loaded SPRP is mainly composed of carbon, oxygen, and platinum, which has a content of around 9 wt.-% (data not shown). The HR-TEM image shown in Figure 8 (d) confirmed that these nanoparticles are crystalline with a lattice distance of 0.22 nm, thus suggesting that they are composed of elemental platinum. As already shown in Figure 6 (b), the carbon–Pt composite gives a similar Raman spectrum to that of SPRP-derived carbon–Pd composite, thereby indicating that carbon in the carbon–Pt composite is also partially graphitized. Compared with the carbon–Pd composite prepared from identical metal-salt concentration and impregnation time, the number of Pt nanoparticles in the carbon–Pt composite is significantly less and the particle size is much smaller. In the XRD pattern of the carbon–Pt composite shown in Figure 6 (a), there is only a weak but wide XRD peak at 40°, which is the characteristic peak of the (111) plane of *fcc* platinum, whereas its ED pattern only shows a halo due to the small size and content of Pt in the composite (Figure 8, e). We think the difference in the metal content present in the carbon–Pd and carbon–Pt composites should be attributed to the oppositely charged nature of $Pd^{2+}$ and $[PtCl_4]^-$. $Pd^{2+}$ is positively charged and is much easier to be attracted by $[COO]^-$ and polarized C–O and C=O bonds in SPRP, whereas $[PtCl_4]^-$ has an electrostatic repulsion to these negatively charged species. Therefore, significantly fewer Pt ions were captured by these active groups, mainly through coordination interactions.

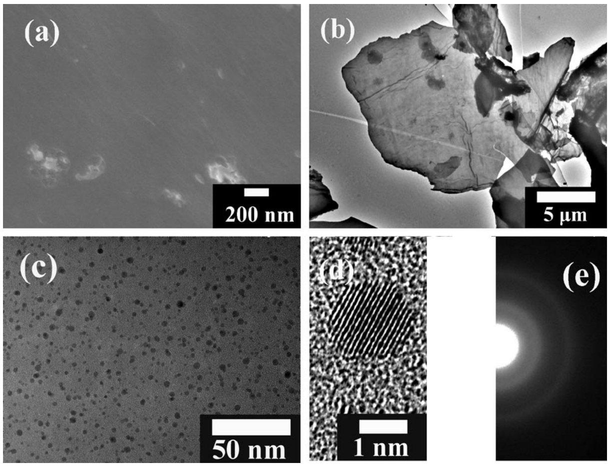

Figure 8. (a) SEM image, (b, c) TEM images, (d) HR-TEM, and (e) SAED pattern of carbonized SPRP impregnated in 1 wt.-% $NaPtCl_4$ solution for 24 h.

The success of the preparation of carbon–Pd and carbon–Pt composite using the wet impregnation plus thermal pyrolysis protocol demonstrates the versatility of this method, and furthermore it is straightforward to imagine that other noble-metal nanoparticles (e.g., Ru, Ag, and Au) supported on biosourced carbon can be obtained through the same method. Moreover, if we start with salts of a less inert metal, for instance, Fe, Cu, Zn, and so forth, composites of carbon and the corresponding metal oxides, which are also intensively used as catalysts for organic synthesis and the growth of nanomaterials, can be prepared using the reported method in which these metal salts will be decomposed in the pyrolysis step and converted to oxides other than elementary metals as in the case of salts of noble metals.

## Conclusion

We investigated a kind of biomaterial, SPRP, which has a macroporous foamlike structure and an ultralow density. We directly pyrolyzed this biomaterial and obtained carbon foam, which was correspondingly extremely light. We disassembled the carbon foam and prepared carbon flakes with nanometer-sized thickness and a large lateral size up to hundreds of micrometers. More importantly, metal ions – for instance, Pd and Pt – were anchored onto the active groups in SPRP and converted to carbon–noble-metal composites in which Pd or Pt nanoparticles with a size of tens of nanometers or several nanometers were uniformly distributed in the carbon nanoflakes. The content of the metal in the composite can be easily tuned over a relatively large range by altering the concentration of metal salts and/or impregnation time. This method is highly versatile, and we believe it can be extended to the preparation of other carbon-based catalyst materials with supported nanoparticles of metals and metal oxides, provided suitable salt sources are used.

## Experimental Section

**General:** Dried SPRP was obtained from a local shop of traditional Chinese medicines in the form of slightly yellowish fibers with a diameter in the range of 3 to 6 mm. As-received SPRP was cut into short rods with a length of 2–4 cm. SPRP rods (1.0 g) were immersed into 0.3 wt.-% or 1 wt-% $Pd(OAc)_2$ (Aldrich) or 1 wt.-% $NaPtCl_4$ (Aldrich) solution (ca. 80 mL) in 1:1 ethanol and deionized water under moderate agitation. After immersion for the desired periods of time, SPRP rods were taken out from the solution and twice rinsed in copious amounts of 1:1 ethanol and water, then dried at 80 °C for approximately 12 h. The $Pd(OAc)_2$- and $NaPtCl_4$-treated and as-received SPRP were directly carbonized at 600 °C for 6 h under a flow of nitrogen. The FTIR spectrum of the pristine SPRP fibers was obtained with a Bruker Tensor 27 spectrometer using the attenuated total reflection (ATR) module. Scanning electron microscopy (SEM) was performed with a Hitachi S4800 microscope operated at 10 keV. The as-received SPRP sample was first sputter-coated with a thin layer of gold–palladium alloy before SEM observation, but all the carbonized samples were examined directly without an additional coating of the conducting layer. The energy-dispersive spectroscopy (EDS) results were obtained with a Bruker EDS system attached to the SEM. For transmission-electron microscopy (TEM), the carbonized samples were ground into powders, followed by dispersion in ethanol under ultrasonication. The suspensions were then deposited on holey carbon-coated copper grids and probed with a JEOL 1010 microscope operated at 100 keV. High-resolution TEM images were obtained with a JEOL 2010 microscope operated at 200 keV. X-ray diffraction (XRD) measurements were performed with a Philips X′pert MRD diffractometer with a cradle and secondary monochromator for Cu-$K_\alpha$ radiation. Raman spectra were measured in reflection mode with a Horiba Jobin Yvon LabRAM HR high-resolution Raman microscope operating with a 632.81 nm laser. The optical photographs were taken with a Kodak DX6340 digital camera.

## Acknowledgments

We gratefully acknowledge Professor Pei Huang for granting us access to the FTIR-ATR equipment in his group. This work is financially supported by the National Natural Science Foundation of China (21004033), the Jiangsu Natural Science Foundation (BK2009358), and the State Key Laboratory of Chemical Resource Engineering.

[1] H. W. Kroto, J. R. Heath, S. C. Obrien, R. F. Curl, R. E. Smalley, *Nature* **1985**, *318*, 162–163.
[2] H. P. Boehm, *Carbon* **1997**, *35*, 581–584.
[3] K. S. Novoselov, A. K. Geim, S. V. Morozov, D. Jiang, Y. Zhang, S. V. Dubonos, *Science* **2004**, *306*, 666–669.
[4] Y. Qin, Z. K. Zhang, Z. L. Cui, *Carbon* **2003**, *41*, 3072–3074.
[5] Y. Wan, Y. F. Shi, D. Y. Zhao, *Chem. Mater.* **2008**, *20*, 932–945.
[6] M. Steinhart, C. D. Liang, G. W. Lynn, U. Goesele, S. Dai, *Chem. Mater.* **2007**, *19*, 2383–2385.
[7] Y. Meng, D. Gu, F. Q. Zhang, Y. F. Shi, H. F. Yang, Z. Li, *Angew. Chem. Int. Ed.* **2005**, *44*, 7053–7059.
[8] Y. Huang, H. Q. Cai, T. Yu, F. Q. Zhang, F. Zhang, Y. Meng, *Angew. Chem. Int. Ed.* **2007**, *46*, 1089–1093.
[9] Y. H. Deng, C. Liu, T. Yu, F. Liu, F. Q. Zhang, Y. Wan, *Chem. Mater.* **2007**, *19*, 3271–3277.
[10] A. Aygun, S. Yenisoy-Karakas, I. Duman, *Microporous Mesoporous Mater.* **2003**, *66*, 189–195.
[11] T. H. Liou, *Carbon* **2004**, *42*, 785–794.
[12] W. M. Qiao, M. Huda, Y. Song, S. H. Yoon, Y. Korai, I. Mochida, *Energy Fuels* **2005**, *19*, 2576–2582.
[13] M. M. Titirici, A. Thomas, S. H. Yu, J. O. Muller, M. Antonietti, *Chem. Mater.* **2007**, *19*, 4205–4212.
[14] O. Ioannidou, A. Zabaniotou, *Renew. Sust. Energy Rev.* **2007**, *11*, 1966–2005.
[15] A. A. Nunes, A. S. Franca, L. S. Oliveira, *Bioresource Technol.* **2009**, *100*, 1786–1792.
[16] F. Cheng, J. Liang, J. Zhao, Z. Tao, J. Chen, *Chem. Mater.* **2008**, *20*, 1889–1895.
[17] F. Zhang, H. Ma, J. Chen, G. D. Li, Y. Zhang, J. S. Chen, *Bioresource Technol.* **2008**, *99*, 4803–4808.
[18] M. S. Balathanigaimani, W. G. Shim, J. W. Lee, H. Moon, *Microporous Mesoporous Mater.* **2009**, *119*, 47–52.
[19] M. Olivares-Marin, J. A. Fernandez, M. J. Lazaro, C. Fernandez-Gonzalez, A. Macias-Garcia, V. Gomez-Serrano, F. Stoeckli, T. A. Centeno, *Mater. Chem. Phys.* **2009**, *114*, 323–327.
[20] F. Zhang, K. X. Wang, G. D. Li, J. S. Chen, *Electrochem. Commun.* **2009**, *11*, 130–133.
[21] S. A. Davis, S. L. Burkett, N. H. Mendelson, S. Mann, *Nature* **1997**, *385*, 420–423.
[22] D. Walsh, L. Arcelli, T. Ikoma, J. Tanaka, S. Mann, *Nat. Mater.* **2003**, *2*, 386–390.
[23] M. B. Dickerson, K. H. Sandhage, R. R. Naik, *Chem. Rev.* **2008**, *108*, 4935–4978.
[24] E. K. Payne, N. L. Rosi, C. Xue, C. A. Mirkin, *Angew. Chem. Int. Ed.* **2005**, *44*, 5064–5067.
[25] J. G. Huang, T. Kunitake, *J. Am. Chem. Soc.* **2003**, *125*, 11834–11835.
[26] S. Sotiropoulou, Y. Sierra-Sastre, S. S. Mark, C. A. Batt, *Chem. Mater.* **2008**, *20*, 821–834.
[27] Y. Wang, Z. M. Liu, B. X. Han, Z. Y. Sun, J. M. Du, J. L. Zhang, *Chem. Commun.* **2005**, 2948–2950.
[28] Z. Miao, Z. J. M. Liu, B. X. Han, Y. Wang, Z. Y. Sun, H. L. Zhang, *J. Supercritical Fluids* **2007**, *42*, 310–315.
[29] Y. Wang, Z. M. Liu, B. X. Han, Y. Huang, G. Y. Yang, *Langmuir* **2005**, *21*, 10846–10849.
[30] D. H. Deng, X. P. Liao, B. Shi, *ChemSusChem* **2008**, *1*, 298–301.
[31] D. H. Deng, H. Wu, X. P. Liao, B. Shi, *Microporous Mesoporous Mater.* **2008**, *116*, 705–709.
[32] C. Chen, E. B. Kennel, A. H. Stiller, P. G. Stansberry, J. W. Zondlo, *Carbon* **2006**, *44*, 1535–1543.
[33] C. M. Leroy, F. Carn, R. Backov, M. Trinquecoste, P. Delhaes, *Carbon* **2007**, *45*, 2317–2320.
[34] S. Li, Q. Guo, Y. Song, Z. Liu, J. Shi, L. Liu, *Carbon* **2007**, *45*, 2843–2845.
[35] M. X. Liu, L. H. Gan, C. Tian, J. C. Zhu, Z. J. Xu, Z. X. Hao, *Carbon* **2007**, *45*, 3045–3046.

[36] M. X. Wang, C. Y. Wang, B. Q. Li, Z. J. Hu, *Carbon* **2008**, *46*, 84–91.
[37] M. Calvo, R. Garcia, S. R. Moinelo, *Energy Fuels* **2008**, *22*, 3376–3383.
[38] Y. Ohmuka, I. Hasegawa, H. Fujisawa, O. Okuma, K. Mae, *Fuel* **2008**, *87*, 2041–2049.
[39] N. Yanna, Z. Peng, G. Zaiping, L. Huakun, Y. Jun, W. Jiulin, *Mater. Res. Bull.* **2009**, *44*, 140–145.
[40] Y. Wang, Z. Liu, B. Han, J. Zhang, T. Jiang, W. Wu, G. Yang, Y. Huang, *Chem. Phys. Lett.* **2003**, *381*, 271–277.
[41] A. C. Ferrari, J. Robertson, *Phys. Rev. B* **2000**, *61*, 14095–14107.
[42] M. Endo, K. Nishimura, Y. A. Kim, K. Hakamada, T. J. Matushita, M. S. Dresselhaus, *Mater. Res.* **1999**, *14*, 4474–4477.

Received: July 26, 2010